ADVANCED MATERIALS INTERFACES
Open Access
www.advmatinterfaces.de

Identifying the Internal Network Structure of a New Copper Isonicotinate Thin-Film Polymorph Obtained via Chemical Vapor Deposition

Lukas Legenstein, Sabina Rodríguez-Hermida, Víctor Rubio-Giménez, Timothée Stassin, Sebastian Hofer, Manuel P. Kainz, Mario Fratschko, Francesco Carraro, Paolo Falcaro, Rob Ameloot, and Roland Resel**

The preparation of thin films is often associated with the appearance of unknown polymorphs, as both the substrate and deposition method can heavily influence crystallization processes. Here, chemical vapor deposition is used to obtain thin films of a copper-isonicotinate (Cu-INA) metal–organic framework (MOF). Starting from copper-based precursor layers (copper oxide and hydroxide), a solid-vapor conversion with vaporized isonicotinic acid in either a dry or humidified atmosphere, yields a new Cu-INA MOF polymorph. It is found that the crystalline order of the precursor layer has a strong impact on the texture of Cu-INA thin films. Furthermore, a novel methodology is introduced to determine the structure of a previously unknown thin-film phase of Cu-INA. Although only a few diffraction peaks are found via synchrotron grazing incidence X-ray diffraction (GIXRD), a triclinic unit cell can be determined, and Patterson functions can be calculated. The latter reveals the position of the copper atoms within the unit cell and the alignment of the INA linkers defining the coordination network structure. This work introduces how the combination of GIXRD data with Patterson functions can be used to identify the structure of an unknown thin-film MOF polymorph.

1. Introduction

Metal–organic frameworks (MOFs) are porous coordination networks composed of metal ions and organic linkers that typically crystallize into various ordered structures.[1] They have shown successful applications in catalysis,[2,3] gas capture, and separation.[4–6] However, some of the least developed applications, such as microelectronic devices,[7,8] require the deposition of homogeneous films onto solid supports.[9] The presence of a surface during framework formation can strongly influence the crystallization process, even inducing the formation of unknown crystal phases. Such unique polymorphs also appear in thin films of purely organic or inorganic compounds[10] and are commonly referred to as substrate-induced polymorphs or thin-film phases.[11] Detailed knowledge of these crystal structures is essential since thin-film phases can have considerably different properties than bulk polymorphs.[12] MOF thin films and specially surface-coordinated MOFs (SURMOFs)[13,14] are known to feature unprecedented polymorphs[15,16] that are not accessible in bulk form and can strongly impact the performance of MOF-based devices.[17,18] Thin-film phases can occur when the MOF building blocks interact with surface groups, such as self-assembled monolayers,[19,15] or when the substrate is covered with a precursor layer (i.e., a metal oxide or hydroxide).[20,21] In addition, the physical state of the reagents that interact with the solid surface (i.e., in solution or the vapor phase) can be a determining factor.[22–24]

Unfortunately, standard crystal structure solution methods are unsuitable for unknown MOF thin-film phases. In contrast to single-crystal or powder X-ray diffraction (XRD) methods,[25] the number of diffraction peaks observed in MOF thin films is

L. Legenstein, S. Hofer, M. P. Kainz, M. Fratschko, R. Resel
Institute of Solid State Physics
Graz University of Technology
Petersgasse 16, Graz 8010, Austria
E-mail: roland.resel@tugraz.at

The ORCID identification number(s) for the author(s) of this article can be found under https://doi.org/10.1002/admi.202202461.

DOI: 10.1002/admi.202202461

S. Rodríguez-Hermida
Servizos de Apoio á Investigación – Universidade da Coruña
Edificio dos Servizos Centrais de Investigación
Campus de Elviña s/n, A Coruña 15071, Spain

S. Rodríguez-Hermida, V. Rubio-Giménez, T. Stassin, R. Ameloot
Centre for Membrane Separations, Adsorption, Catalysis and Spectroscopy
Katholieke Universiteit Leuven
Celestijnenlaan 200F, Leuven 3001, Belgium
E-mail: victorrubio.gimenez@kuleuven.be

F. Carraro, P. Falcaro
Institute of Physical and Theoretical Chemistry
Graz University of Technology
Stremayrgasse 9, Graz 8010, Austria

usually too small to solve the structure and calculate the electron density distribution within the crystallographic unit cell. Also, in the case of powder methods,[26] the geometry of the internal network is challenging to identify since the exact chemical composition (e.g., the ratio between metal nodes and linker molecules) is not precisely known. Moreover, simple principles related to molecular packing, such as the close-packing principle for molecular crystals or the mass density rule, cannot be applied.[27,28]

In order to tackle this issue, we present a methodology for crystal structure elucidation of a MOF thin-film phase based on the concept developed for films of molecular crystals, through a combined experimental and theoretical approach.[29,30] Grazing incidence X-ray diffraction (GIXRD) is the method to determine the crystallographic unit cell and the structure factors of individual Bragg peaks. Here, we determined the internal framework structure using Patterson functions in combination with the knowledge of the chemical structure of the linker molecules.

As a case study, we chose a well-known MOF system known as copper-isonicotinate (Cu-INA). The INA linker can coordinate metal ions through a carboxylate group on one end and a pyridinic nitrogen on the other. These different coordination sites result in a rich phase behavior of MOFs based on copper nodes and INA linkers: molecular clusters with embedded water;[31] 1D chains with hydrogen bonds in between;[32,33] 2D,[34] and 3D networks with empty pores[35] and with pores accommodating water or alcohols.[35–37] The copper nodes can be either a single atom,[35] copper paddlewheels formed with four carboxylates,[38,39] or a combination of both.[40–42] In addition, structures containing complex nodes[43] and even copper-oxo chains[44] have been observed. The coordination mode of the single copper nodes is frequently pyramidal,[35] but it can also be double pyramidal,[31,45] or a mixture of both.[46] The number of copper atoms within a crystallographic unit cell and the copper:INA ratio can vary significantly, from 1 to 6 and between 2 and 0.66, respectively. This structural and compositional diversity adds to the challenge of solving the structure of a new Cu-INA polymorph.

Here, we present the preparation of an unprecedented Cu-INA MOF thin-film phase via chemical vapor deposition (CVD). In addition to being a new Cu-INA polymorph, our thin films have a strong preferred crystal orientation relative to the substrate surface (uniplanar texture). We also propose a new method to determine its crystal structure based on the analysis of GIXRD data in combination with the calculation of Patterson functions.

2. Results and Discussion

2.1. Thin Film Preparation

The preparation of Cu-INA thin films via CVD involves a two-step process, as depicted in **Figure 1**a. In the first step, the Cu-based precursor materials were deposited on planar substrates (silicon wafers). Two different precursor materials were used: copper oxide layers obtained by sputtering and copper-hydroxide nanobelts uniaxially aligned by solution processing (see section 2.3).[47] Copper oxide layers with three different thicknesses were sputtered with ≈10, 20, and 100 nm, as determined via ex situ ellipsometry (Figure S1, Supporting Information). In the second step (Figure S2, Supporting Information), the substrate was exposed to INA ligand vapor at temperatures between 150 and 200 °C, which triggered the solid-vapor reaction that forms Cu-INA. This conversion can be carried out in the presence or absence of water vapor (humidified or dry conditions). The water content in the reaction atmosphere has been

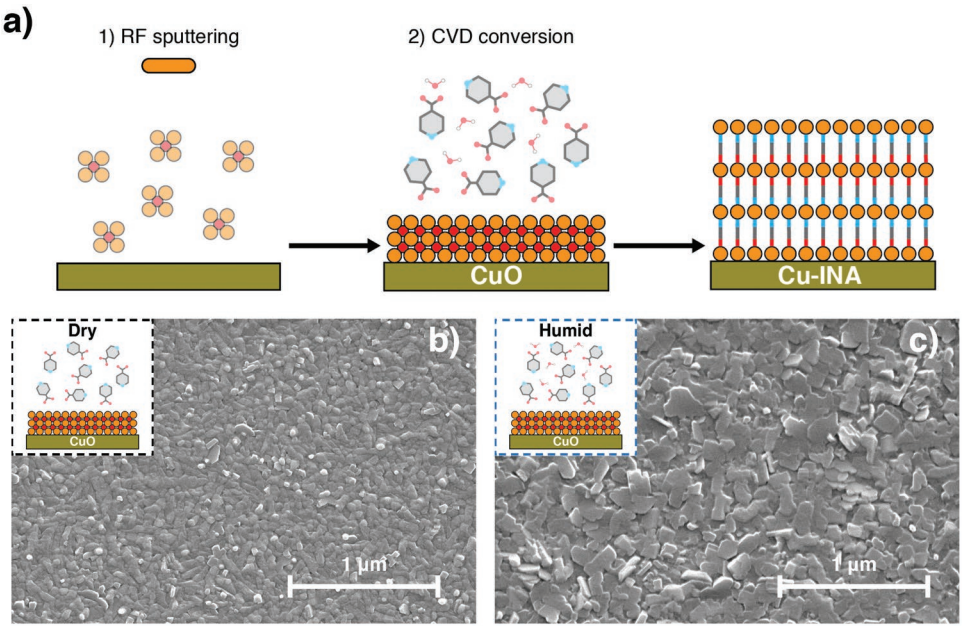

Figure 1. a) Scheme of the deposition procedures of Cu-INA thin films with uniplanar textures: 1) A copper oxide precursor layer is deposited via RF sputtering, followed by 2) exposure to INA vapor under dry or humid conditions to obtain the final Cu-INA thin film. SEM images of Cu-INA samples prepared at 200 °C under b) dry or c) humid conditions from 100 nm copper oxide layers reveal the different crystalline morphologies.

reported to play a central role in MOF crystallization, even acting as a template to form certain polymorphs in MOF-CVD.[24,48–51] As visible in Figure 1b,c, scanning electron microscopy (SEM) images of the resulting Cu-INA thin films converted at 200 °C from sputtered copper oxide show homogeneous surfaces composed of nanocrystallites for all cases. Comparable morphologies are found for films converted at 150 and 175 °C (Figure S3, Supporting Information). However, there is a clear difference in the morphologies of thin films prepared under dry (Figure 1b and Figure S4a,b, Supporting Information) or humid (Figure 1c and Figure S4c,d, Supporting Information) conditions. The presence of water vapor yields a rougher surface with larger crystallites, while its absence produces randomly distributed and smaller particles. This is in line with previous protocols for the fabrication of thin films bases on different types of MOFs.[49,52]

2.2. Cu-INA Thin Films with Uniplanar Texture: Sputtered CuO Precursor

In the first step, specular XRD was performed on samples prepared at 200 °C in the presence and absence of water vapor and using the same range of initial copper oxide precursor thicknesses: 100 nm (blue), 20 nm (orange), and 10 nm (yellow). As visible in **Figure 2**a, all six diffraction patterns show strong Bragg peaks at 1.42 and 2.84 Å^{-1}, and a weak one at 2.13 Å^{-1}. These three peaks represent higher-order reflections of the same net plane series with an interplanar distance of 8.87 Å. Less pronounced diffraction patterns were found for films prepared at lower conversion temperatures (Figure S5, Supporting Information). Qualitative phase analysis was performed by comparing the calculated peak positions of precursor and previously reported Cu-INA compounds with the experimental diffractograms. These three peaks did not match to any crystalline phases of the precursor materials (copper oxides or INA), nor any reported bulk Cu-INA structures. Therefore, these diffraction peaks were attributed to an unknown Cu-INA polymorph. Notably, the sharp peak at 2.32 Å^{-1} and the shoulder at 2.35 Å^{-1} arise from the 200 diffraction peak of the silicon substrate due to dynamic scattering.[53] Finally, additional diffraction features are observed in samples prepared from 100 nm precursor layers (blue lines) at 2.51 and 2.53 Å^{-1}, this peak is assigned to the 002 Bragg peak (2.49 Å^{-1}) of unreacted monoclinic CuO precursor (see Figure S6, Supporting Information),[54] in line with our previous spectroscopic studies of equivalent sputtered CuO precursor layers, which show a dominant presence of Cu^{II}.[55,56] The peak is absent in the 20 nm and 10 nm samples, indicating that, in these cases, the complete CuO precursor layer was converted to Cu-INA. This self-limiting behavior is typical in CVD synthesis and has been observed for other thin-film oxide precursors.[48–50]

According to the crystal structure solution based on GIXRD data (see below), Cu-INA peaks could be assigned to the Laue indices *hhh*. The 111 and 333 peaks show systematically lower intensities next to the 222 and 444 peaks. The observation of a peak series arising from only one specific interplanar distance reveals that the crystallites in the film have a strong preferred orientation with the (111) plane parallel to the substrate. The diffraction patterns of dry samples appeared slightly different to the humified ones, which reveal only minor differences in the crystal structures: First, the 111 peak is only detected in the 10 nm sample. Second, the 333 peak can only be seen for the 20 nm sample. Third, for the 10 and 20 nm samples, an additional peak appears at 1.83 Å^{-1}. Finally, all Cu-INA MOF peaks of the 10 nm sample are shifted to higher q_z values by a slight margin of 0.014 Å^{-1} for the 444 peak (indicating a net plane distance 0.011 Å smaller), compared to the peak positions of the other samples. In contrast, the diffraction peaks of the humidified samples are more prominent and show identical intensity ratios. In conclusion, humidified conditions yield a defined thin-film polymorph with a strong preferred orientation.

Next, synchrotron GIXRD experiments were performed on all samples, and reciprocal space maps (RSMs) were calculated from the 2D detector images. RSMs of two thin film samples prepared under humidified and dry conditions from 100 nm CuO precursor are shown in Figure 2. These are

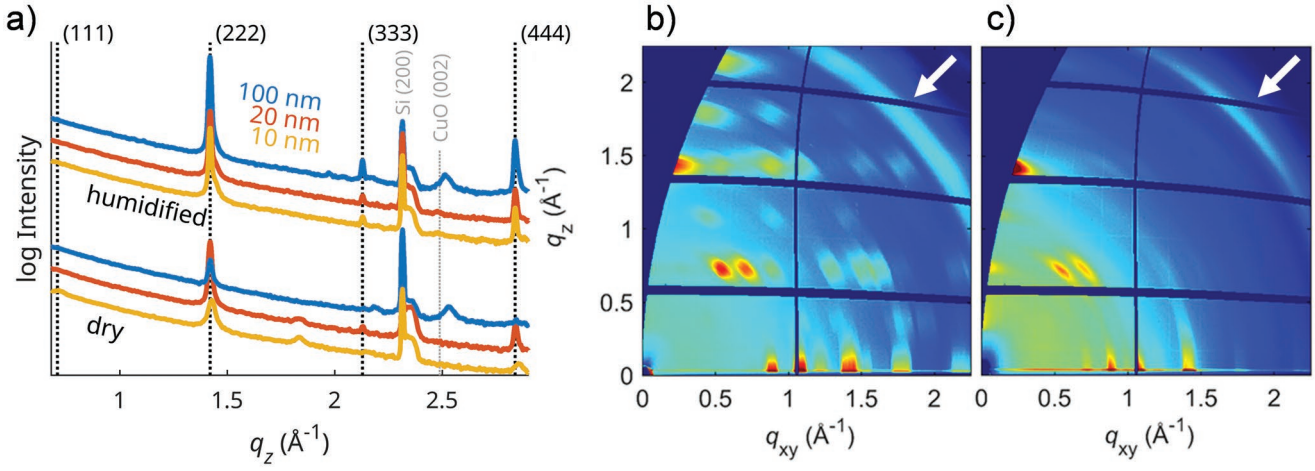

Figure 2. a) Specular XRD of Cu-INA thin films prepared from different CuO precursor thickness under dry and humidified conditions. Curves are vertically shifted for comparison. b,c) Reciprocal space maps of Cu-INA thin film samples prepared from 100 nm CuO precursor thickness obtained from GIXRD measurements at an incident angle $\alpha_i = 0.2°$. Precursor layers were converted at a temperature of 200 °C under humidified (b) and dry conditions (c). Intensities are plotted on a linear scale. Arrows denote diffraction features from the remaining CuO precursor layer.

representative of all samples since comparable peak patterns are found for Cu-INA films converted from thinner precursor films (10 and 20 nm). Rotating the sample did not change the number of observed diffraction peaks, and the intensity ratios between the peaks did not shift, indicating a random in-plane alignment of the crystallites. GIXRD patterns of films prepared at lower conversion temperatures and with smaller precursor layer thicknesses are shown in Figure S5 (Supporting Information). The observed texture of the Cu-INA crystallites can be classified as a uniplanar texture according to the scheme of Heffelfinger–Burton or simply as a fiber texture.[57,58]

As depicted in Figure 2, these RSMs show Bragg peaks with a spot-like character, meaning that these appear within small arcs due to the mosaicity of the Cu-INA crystals. At the center of the arcs, the diffraction peaks have a sharp character with considerably higher intensity. The two depicted RSMs are comparable in terms of peak positions (q_{xy} and q_z), but the larger extension of the arcs in the dry samples reveals that the mosaicity of the humidified sample is smaller. This result indicates that the preferred orientation of the (111)-oriented Cu-INA crystals relative to the substrate surface is better defined in the case of the humidified sample. Besides, the dominant diffraction peaks of Cu-INA and of the remaining CuO are visible in the RSMs. A ring-like feature (marked by white arrows) appears at $q = 2.49$ Å^{-1} due to the 002 Bragg peak, in consonance with specular XRD observations (Figure 2a).

Compared to the surface sensitive RSM recorded at an incident angle of $\alpha_i = 0.2°$, the maxima in the diffraction pattern recorded at $\alpha_i = 3°$ were only weakly visible. Therefore, the summation of patterns recorded during sample rotation was necessary, and the resulting summed RSM can be seen in **Figure 3**a. Radial smearing of the Bragg peaks was reduced by the relatively high incidence angle in combination with the improved signal due to summation. The Bragg peaks appear as localized and sharp maxima, and their positions can be determined precisely. Therefore, this RSM was used for indexing the observed Bragg peaks since the peaks appear considerably sharper, allowing an improved accuracy in the determination of the lattice constants of the crystallographic unit cell. The coordinates (q_{xy}, q_z) of 22 Bragg peaks, in combination with the positions of two specular diffraction peaks (0, q_z), were provided as input for the indexing software. The output of the software is a combination of Miller's indices of the crystallographic plane parallel to the substrate (the so-called contact plane) and the lattice constants of the crystallographic unit cell. A (111) preferred orientation is found together with a triclinic unit cell (**Table 1**). Lattice constants, as well as Miller's indices of the contact plane, are used to calculate the position of the diffraction peaks within the experimental RSM. The calculated positions are given in Figure 3a by diagonal crosses together with the corresponding representative Laue indices.

No match for the crystallographic unit cell could be found with any reported structure of the Cambridge Structural Database, considering INA-based MOFs with copper or any other transition metal like Zn, Cd, or Fe as a metal node. Therefore, the investigated structure can be considered an unknown, novel Cu-INA polymorph.

Based on the typical stoichiometry and density of Cu-INA MOFs, the unit cell with a volume of 1808.33 Å^3 certainly contains several copper atoms and INA molecules. However, the obtained unit cell dimensions do not trivially reveal an obvious spatial distribution of copper and INA fragments. Moreover,

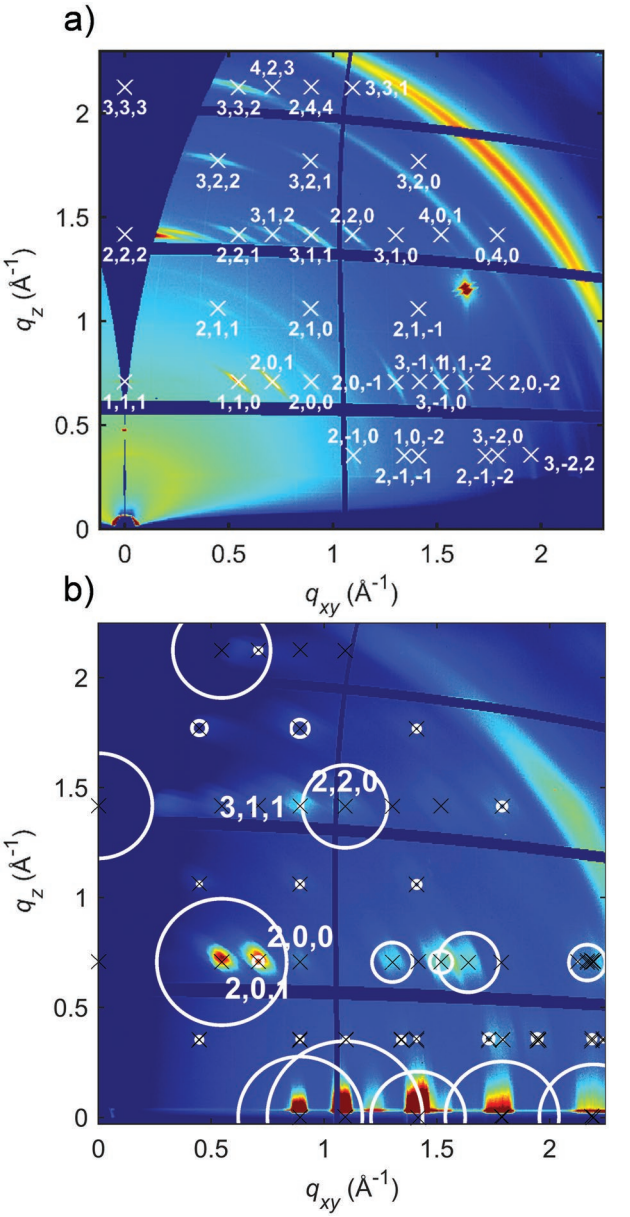

Figure 3. RSMs of a Cu-INA thin film prepared from 100 nm CuO precursor layer under humidified conditions calculated from GIXRD measurements at incidence angles of a) 3° for indexing and at b) 1° for proper observation of in-plane diffraction peaks at different q_{xy} positions and $q_z = 0$ Å^{-1}. Diagonal crosses and the center of circles give the positions of the diffraction peaks (a,b), and the areas inside the circles show the square of the structure factors of the proposed structure solution.

the exact chemical composition, i.e., the number of copper atoms and the fraction of INA molecules, is unknown. Therefore, classical approaches to crystal structure elucidation based on a limited number of diffraction peaks are unsuitable. And, methods such as filling the crystallographic unit cell with a defined number of structural units or a close-packing analysis by molecular dynamics simulations cannot be applied.[11] Therefore, other approaches for solving the crystal structure have to be developed.

The pronounced contrast in electron density within a MOF unit cell results in a strong variation of the intensities of the

ADVANCED MATERIALS INTERFACES
Open Access
www.advmatinterfaces.de

Table 1. Details of the crystallographic unit cell of the thin-film polymorph of Cu-INA as obtained by indexing the RSM derived from GIXRD measurements. The crystal symmetry, the crystallographic plane parallel to the substrate surface, the lattice constants as well as the volume of the unit cell are given.

Crystal symmetry	Preferred orientation	a [Å]	b [Å]	c [Å]	V [Å^3]
Triclinic	(111)	12.541	12.541	14.503	1808.33
		α [deg.]	β [deg.]	γ [deg.]	
		64.47	64.47	90.0	

observed Bragg peaks. Moreover, the distribution of the peak intensities gives implicit information about the arrangement of the molecular units and metal nodes within the unit cell. The variation of the electron density caused by the presence of "heavy atoms" and by the presence of "light atoms" results in distinct maxima appearing in Patterson functions. Correlations between heavy and light atoms can therefore be categorized into distinguishable maxima arising from heavy-heavy, heavy-light, and light-light atomic pairs. The heavy-heavy maxima would correspond to the largest function values, proportional to Z^2_{metal}, with Z_{metal} as the atomic number of the heavy (metal) atom. The heavy-light maxima would also be noticeable, albeit smaller and proportional to roughly $Z_{\text{metal}}*Z_C$, with Z_C as the atomic number of the light (carbon) atom ($Z_C = 6$). Finally, the light–light maxima would contribute only little to the Patterson function. In our case, the light atoms come from the INA molecule and involve oxygen, nitrogen, carbon, and hydrogen atoms. In summary, the "Heavy Atom Method" is based on the identification of maxima in the Patterson function to identify regions with a high electron density, which are assigned to the position of the metal atoms.

The quantitative analysis of peak intensities, namely, calculating a Patterson function, is based on GIXRD experiments recorded at an incident angle of 1°. The corresponding RSM is depicted in Figure 3b. An improved data analysis is possible, since intensity amplification of in-plane peaks is reduced.[59] The observed intensities are corrected for the calculation of Patterson maps in terms of geometrical factors like polarization factor, Lorentz factor, and peak multiplicity.

The calculated Patterson function is shown in **Figure 4**a. For visualization, the relative atomic coordinates $u\ v\ w$ are chosen between −0.25 and 1.25 (in fractional coordinates). A threshold (mean value of the Patterson function with an added variance) was applied, and function values below were set to appear transparent to provide an unobstructed view of relevant maxima. Only function values above the threshold are discussed here.

Besides the origin peaks at the corners, two distinguished high-intensity maxima could be identified at 1/2,1/2,0, marked by orange color and at 1/4,3/4,1/2 marked by purple color, with the symmetry-equivalent maximum at 3/4,1/4,1/2. Maxima in the Patterson function represent relative coordinates between atoms or interatomic vectors in absolute coordinates. The transition from relative coordinates to absolute atomic positions is obtained by the superposition of the interatomic vectors: adding together any pair of two vectors should result in a vector that is also part of the set. Considering only the maxima of the Patterson function reveals the absolute position of four copper

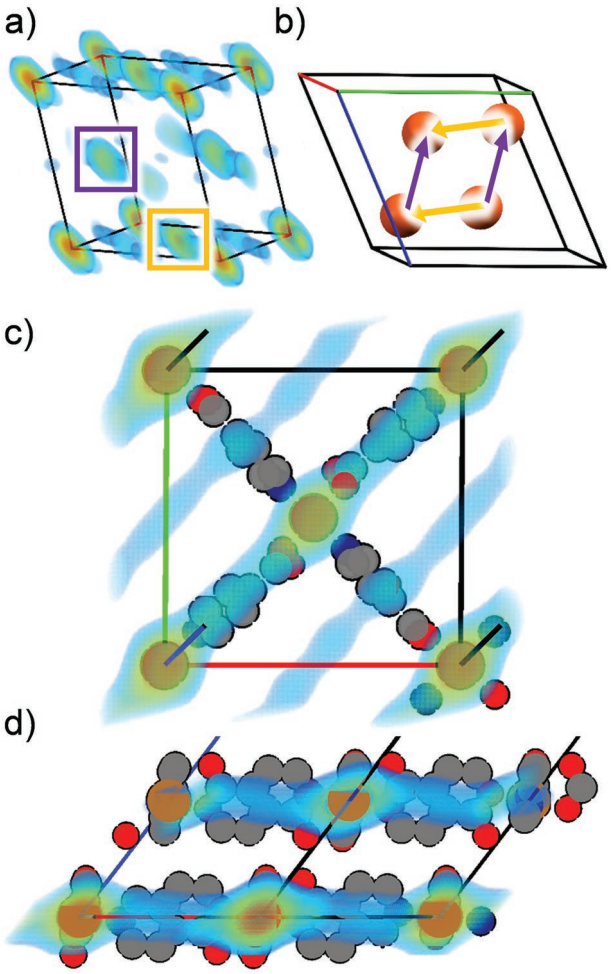

Figure 4. a) Patterson function calculated from GIXRD data, values below a threshold are not visualized. b) absolute positions of copper atoms within the crystallographic unit cell derived from the Patterson maxima with orange and purple arrows indicating the interatomic vectors highlighted in panel (a). c,d) Patterson function calculated from GIXRD data together with a hypothetical test structure viewed along two distinct crystallographic directions: [001]* and [−110]. The Patterson function is only plotted for values larger than a threshold given in the text and hydrogen atoms of the test structure are omitted.

atoms found within the crystallographic unit cell, which are depicted in Figure 4b in absolute coordinates together with the corresponding copper atoms.

Additional interesting features are visible within the Patterson maps. Figure 4 shows two different views, one along the [001]* direction viewing the (001) plane (Figure 4c) and the second along [−110] direction viewing the (−110) plane (Figure 4d). Between the maxima of the Patterson functions, which are mainly originated from the copper atoms, additional elongated stretches of increased function values are found. In the first step, we analyzed the prominent maxima at 1/2,1/2,0, which corresponds to the copper atoms at 1/8,3/8,1/4 and 5/8,7/8,1/4 in the crystallographic unit cell. We found a distance of 8.87 Å, which corresponds quite well with the characteristic binding distance of copper atoms by an INA linker for other Cu-INA polymorphs.[35] A second linker coordination with identical distance occurs orthogonally to the previously described one by using ±1/2,±1/2,0 as

the second vector identified by the Patterson function. Both observed linker coordination bonds connect copper atoms located in the (001) plane so that a 2D framework is formed. A direct connection via an INA linker between neighboring 2D networks could not be identified, neither by characteristic copper–copper distances nor by stretches in the Patterson function (see Figure 4d).

In the next step, we built a hypothetical model of our Cu-INA MOF. Linker molecules of the proposed test structure are plotted superimposed over the Patterson function. The linkers are placed between copper atom positions, according to our findings. Copper positions coincide with maxima of the Patterson function while linker molecules align along the extended stretches of intensity in between. The internal framework consists of copper atoms connected in 2D by four INA linkers roughly within the same plane, two with the pyridine and two with the carboxylic group. Systematic absences of intensities (e.g., for the 111 peak) in the diffraction pattern imply the necessity of mirrored electron densities along the linker axes. Therefore, we decided to attach the INA molecules with nitrogen atoms along one line and orthogonal to the oxygen atoms along the other line.

A comparison of a calculated diffraction pattern with the experimental RSM is depicted in Figure 3b. White circles plotted over the intensity corrected RSM indicate the magnitude of the squared structure factor of the proposed test structure. All the high-intensity in-plane peaks (located at $q_z = 0$) fit remarkably well with the recorded intensities. At elevated q_z values, our calculation also reproduces quite well the alternating rows of high intensity (located at $q_z = 0.708$ and 1.416 Å^{-1}) and low-intensity Bragg peaks ($q_z = 0.354$, 1.062, and 1.770 Å^{-1}). However, in a few cases, discrepancies appear. These exceptions are denoted by their Laue indices: detectable intensities are not found for 200, 201, and 311, while the 220 structure factor appears too large.

The crystallographic unit cell, together with the atomic positions of the copper atoms and the proposed linker atoms in between them, are gathered in a crystallographic information file available via the Supporting Information. An inversion symmetry is implemented by using the space group *P-1*. In total, we found four copper atoms and eight INA linkers within the unit cell, which results in a mass density of 1.13 g cm^{-3}.

2.3. Cu-INA Thin Films with Axial Texture: $Cu(OH)_2$ Nanobelts Precursor

As mentioned in Section 2.1, apart from sputtered CuO, we also used solution-processed copper-hydroxide nanobelts as precursors. As depicted in **Figure 5**a, these nanobelts were first synthesized and transferred to a silicon substrate following a previously reported procedure,[47] and then subjected to the same CVD treatment under dry or humidified conditions. In contrast to the sputtered layers, the nanobelts are unstable at elevated temperatures since a transition to copper oxide appears at temperatures above 150 °C.[54] This well-known topotactic transition results in copper oxide that is crystallographically related to the initial copper hydroxide, meaning that the axial texture of the nanobelts is preserved. After conversion with INA at 175 or 200 °C, SEM analysis shows the formation of Cu-INA nanocrystallites along the nanobelts with similar morphologies to the sputtered CuO samples. Dry conditions result in more homogeneous coatings of elongated strips (Figure 5b and Figure S7b, Supporting Information), while a humidified environment yields larger crystallites with sharper edges, resulting in rougher coatings, as visible in Figure 5c and Figure S7c (Supporting Information).

In the first step, the distribution of CuO crystallites within the thin film samples was investigated. Specular XRD reveals the presence of monoclinic CuO (Figure S7a, Supporting Information). XRD pole figures are taken at $q = 2.48$ Å^{-1} for investigation of the spatial distribution of 002 and 11-1 pole densities. The result is depicted in Figure 5d. Enhanced pole densities are found along $\phi = 0°$ and 180° located with a maximum in the center of the pole figure. Additional arcs are found at around $\psi = 65°$ located at $\phi = 100°$ and 280°. These two features of enhanced pole densities are assigned to 200 and 11-1 Bragg peaks, respectively. The texture of the CuO film can be classified as axial texture, with the [1–20] direction (~$[1\text{-}10]^*$ in the reciprocal lattice) parallel to a defined direction along the substrate surface.[57]

Remarkably, the Cu-INA crystal structure in the nanobelt samples is identical to the already observed one prepared on sputtered CuO layers and does not show significant differences with the conversion temperature, as confirmed by specular XRD and GIXRD (Figure S7a,d–f, Supporting Information). In a subsequent step, we analyzed the texture of the Cu-INA crystallites by pole figures investigating the pole densities of 222 and 002 Bragg peaks (Figure 5e,f, Supporting Information). An axial texture of the Cu-INA crystallites is observed with the [002] direction along a distinct substrate azimuth. The same type of texture is observed for the converted CuO layer from $Cu(OH)_2$ nanobelts. This similarity allows to determine the epitaxial relationship between the CuO crystallites from the substrate with the vapor phase grown Cu-INA crystallites expressed in terms of coincidence ($\|$) of planes and directions: $(111)_{\text{Cu-INA}} \,\|\, (002)_{\text{CuO}}$ and $[001]^*_{\text{Cu-INA}} \,\|\, [1\text{–}10]^*_{\text{CuO}}$. Please note that the directions are given in the reciprocal lattice (marked by asterisks) for easier traceability.

2.4. Thin Film Crystal Order

The combination of the crystal structure solution with the observed textures reveals the alignment of the framework structure relative to the substrate surface. The obtained network structure of Cu-INA is depicted in **Figure 6**. The MOF crystals arrange with the (111) plane parallel to the substrate surface, which could be either silicon oxide from the wafer or remaining CuO from the precursor layer. 2D MOF sheets are arranged parallel to each other and perpendicularly (upright standing) to the substrate (Figure 6a). The pore structure within an individual layer is formed by a quadratic arrangement of copper atoms separated by 8.9 Å from each other. Since the exact conformation of the INA molecules is not known, the actual pore size cannot be crystallographically determined. The complete pore arrangement within the 3D

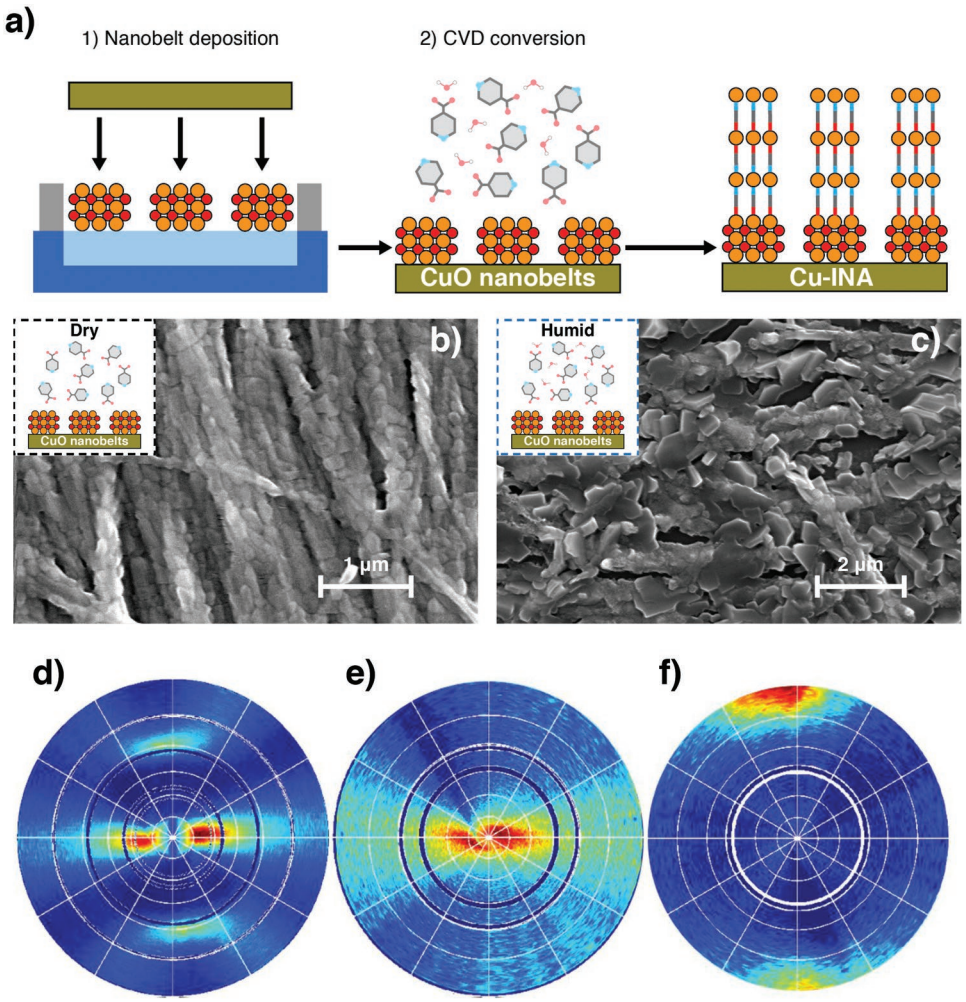

Figure 5. a) Scheme of the deposition procedure of copper hydroxide nanobelts and subsequent conversion to CuO nanobelts coated with Cu-INA: 1) Transfer of oriented copper hydroxide nanobelts floating in water to a silicon substrate; followed by 2) exposure to INA vapor under dry or humid conditions to obtain the final Cu-INA layer. SEM images of samples prepared at 175 °C under b) dry or c) humid conditions reveal the different crystalline morphologies. d) XRD pole figures for mapping of crystal distributions taken at $q = 2.48$ Å^{-1} to visualize the spatial distribution of 002 and 11-1 pole densities of CuO crystallites obtained after a phase transition from copper-hydroxide nanobelts and of Cu-INA crystallites (dry conditions, 175 °C) taken at e) $q = 1.42$ Å^{-1} for 222 poles and f) $q = 1.09$ Å^{-1} for 002 poles. White rings are plotted in φ – steps of 15°, black rings appear due to gaps in the used 2D detector.

MOF structure is visualized in Figure 6b: neighboring layers show diagonally displaced pores.

Besides the already mentioned missing knowledge of the exact conformation of the INA molecules, another insufficient fact is the stabilization of neighboring layers. The average distance of two layers is given by $d_{001}/2 = 5.75$ Å with d_{001} being the interplanar distance between the (001) planes. The resulting distance between linker atoms of neighboring layers is too small for layer stabilization by van der Waals interaction. A reasonable explanation could be that water molecules may connect the layers via hydrogen bonds. Water was intentionally used within the synthesis process and the crystallographic quality of the Cu-INA films was considerably better than the film prepared without added water vapor. Moreover, there are examples of Cu-INA MOFs where water molecules stabilize 3D networks.[31,60] Nevertheless, we are confident that the main structural features of this Cu-INA polymorph were correctly identified. Although deviations may arise from the unknown features of the internal MOF structure regarding the linker molecules, the agreement of the calculated diffraction pattern with the experimental results is reasonable.

The successful use of Patterson functions for solving thin-film crystal structures is limited by a sufficient number of independent diffraction peaks in relation to the number of heavy atoms in the crystallographic unit cell. If the available number of peaks is too small (i.e., in case of very thin films), no clear maxima will appear in the Patterson maps, so that defined positions of the heavy atoms cannot be found. However, the used "Heavy Atom Method" could be further improved by superior Patterson maps (e.g., by including a larger number of diffraction peaks). An improved interpretation of the current Patterson

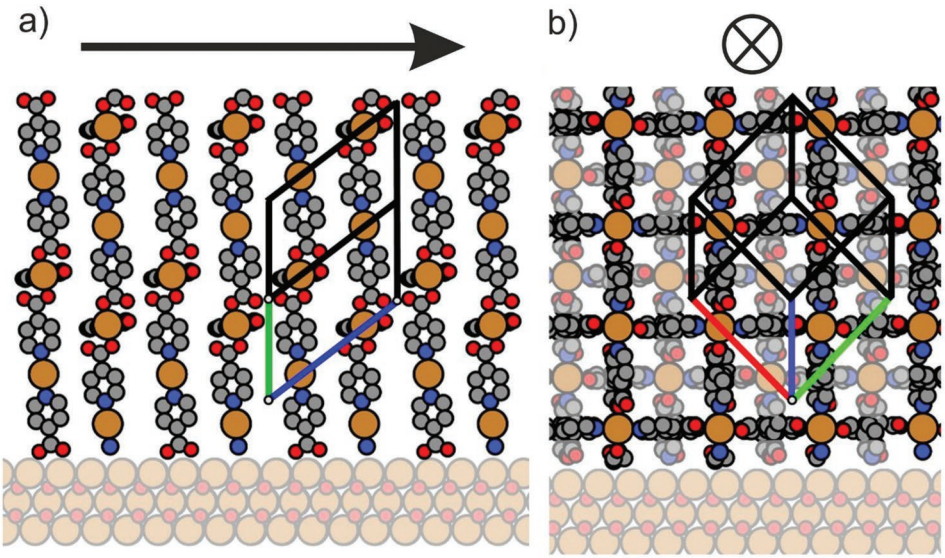

Figure 6. a,b) Arrangement of the Cu-INA MOF structure relative to the CuO surface in a front and in a side view. The 2D layers are arranged perpendicular to the substrate surface and plotted along (a) and perpendicular to the 2D MOF layer (b). The front layer is plotted in full color, while faded colors are used for the layer behind (b). The crystallographic unit cell is plotted in both cases. The epitaxial coincidence $[001]^{*}_{\text{Cu-INA}} \parallel [1\text{-}10]^{*}_{\text{CuO}}$ is given in terms of crystallographic directions in reciprocal space by arrows in the horizontal direction (a) and perpendicular to the plane of projection (b).

map would be possible by a "Fragment Search," where one would calculate the Patterson map of a known part of the structure from theoretical structure factors and search for that signature within the experimentally determined Patterson map.[25] Since linker molecules and potentially even some coordination cluster geometries are known, this adaption may be successfully applied for MOFs.

3. Conclusion

Thin films of a new Cu-INA MOF polymorph were prepared by CVD conversion of two different types of precursor layers (copper oxide films and copper-hydroxide nanobelts) in INA vapor at elevated temperatures. Conversion temperatures of 150–200 °C and adding small quantities of water lead to defined Cu-INA crystals with defined orientation relative to the substrate surface. The use of two different types of precursor layers results in the same crystal structure of the Cu-INA MOF but with two different types of preferred orientations: uniplanar and uniaxial texture. Crystallographic studies revealed the appearance of an unknown polymorph with 22 independent Bragg peaks observed by a combination of specular XRD and synchrotron GIXRD. Known strategies for solving crystal structures were applied and extended towards Patterson functions to determine the positions of the copper atoms. In addition, elongated streaks are observed within the Patterson function, which could be assigned to the INA linker molecules connecting the copper atoms. Thus, the framework structure of a 2D Cu-INA MOF could be identified with four copper atoms and eight linker molecules within the crystallographic unit cell. The knowledge of the crystal structure, together with the strong preferred orientation of the Cu-INA crystallites, reveals the alignment of the MOF pores perpendicular to the substrate surface. We believe that this crystal structure solution methodology overcomes some of the obstacles inherent to MOF thin film samples. This strategy could significantly help material scientists by facilitating the resolution of thin-film polymorphs, thus bridging the gap with single crystal or powder XRD methods.

4. Experimental Section

Materials and Reagents: Isonicotinic acid (99%) was purchased from Acros. All other reagents and solvents were purchased from a commercial supplier and used as received.

Thin Film Synthesis: Thin films of Cu-INA were prepared on ⟨100⟩ silicon wafers with a native oxide film on top. For the first sample series, a layer of CuO was deposited via physical vapor deposition using a magnetron sputter coater and a CuO target. For a second sample series, copper-hydroxide nanobelts were synthesized by a previously reported wet-chemical method with slight modifications, spread at a water surface, and the uniaxially aligned nanobelts were manually transferred to a silicon substrate.[20] For the conversion of the two different types of precursor layers into a MOF thin film, samples were placed in a Schlenk tube next to a glass boat containing 500 mg of isonicotinic acid and evacuated under dynamic vacuum (≈10^{-2} mbar) for 20 min. The closed, evacuated tube was placed inside a convection oven at temperatures between 150 and 200 °C for 16 h. For some experiments, a humidified atmosphere was created in a double-neck Schlenk tube in which 100 µL of water was added before the heating. After the solid-vapor reaction, the samples were removed from the Schlenk tube and subsequently activated at 200 °C for 10 min to remove water and unreacted linkers.

CuO RF Sputtering: Depositions were performed in a Balzers RF-sputter coater (baseline pressure of 2×10^{-5} mbar) at an argon partial pressure of 2–3 $\times$ 10^{-3} mbar at 120 W. To guarantee an homogenous deposition from sputtering 3-in. targets, the substrates were rotated tangentially over the targets (target–sample distance was ≈4 cm), which also ensures a low, controllable deposition rate (≈6 nm min^{-1}). Multiple substrates were coated simultaneously. The CuO thickness was varied between 10 and 100 nm through control over the deposition time and was determined via spectroscopic ellipsometry.

Spectroscopic Ellipsometry: Measurements were performed either with an M-2000X (J.A. Woollam, USA; 65° incident angle, spectral range 245–1000 nm) or an iSE (J.A. Woollam, USA; 70° incident angle, spectral 400–1000 nm) instrument. Optical modeling was performed using the CompleteEASE (v6) software (J.A. Woollam, USA). Data for CuO films was fitted using a Tauc–Lorentz model.

Scanning Electron Microscopy: Images of samples sputter-coated with 2 nm of Pt were recorded using an FEI XL30FEG instrument operating at an accelerating voltage of 10 keV.

Specular X-Ray Diffraction: Diffractograms were collected with an Empyrean PANalytical system using a sealed copper tube. On the primary side, the system is equipped with a multilayer mirror for parallelizing the primary beam and monochromatization (CuKα with λ = 1.5418 Å). In addition, a 1/8° divergence slit and a 4 mm beam mask were used. At the secondary side, a 7.5 mm antiscatter slit and a 0.02 rad Soller slit were used in combination with a PIXcel 3D area detector operating in scanning line mode. Due to the specular geometry, the scattering vector q has only a z-component (perpendicular to the sample surface) so that the scattering angle 2θ is transformed to $q_z = 4\pi/\lambda \sin(2\theta/2)$ for an easy comparison with other XRD experiments.

Grazing Incidence X-Ray Diffraction: Measurements were performed at the beamline XRD1 of the Elettra synchrotron (Trieste, Italy). The primary X-ray beam had a size of 0.5 mm × 0.5 mm and a wavelength of 1.40 Å. The samples were mounted on a goniometer with κ– geometry so that the angle of the primary X-ray beam relative to the substrate (angle of incidence α_i) could be chosen together with sample rotation (angle ϕ) around the surface normal (rotating GIXRD). The incidence angle α_i was varied from 0.2° to 3°. The diffracted beam was detected with a stationary Dectris Pilatus 2M detector. Integration of the diffracted intensities during rotation of the sample considerably improves the statistics, and diffraction patterns integrated along a full rotation of 360° were labeled as such when presented. Pole figures were calculated from rotating GIXRD experiments using the individual diffraction patterns at different sample rotation angles ϕ, 180 diffraction patterns were collected in steps of 2°.[61]

For further processing of the experimental data, the beamline was calibrated in terms of sample–detector distance and detector tilts with polycrystalline LaB_6. The detector images were converted into reciprocal space coordinates by the open-source package *GIDVis*.[61] RSMs were labeled by the out-of-plane component of the scattering vector q_z, perpendicular to the sample surface and $q_{xy} = \sqrt{q_x^2 + q_y^2}$ as the in-plane component aligned along the sample surface. The total length of the scattering vector q can be determined by $q = \sqrt{q_{xy}^2 + q_z^2}$. Peak positions and peak intensities were determined from the reciprocal space maps by fitting a 2D Gaussian function to the underlying intensity map, thus allowing to assign peak coordinates precisely and calculate the intensity elevation over the background. The peak intensities were corrected in terms of Lorentz factor, polarization factor, and multiplicity to elucidate the square of the structure factor ($|F_{hkl}|^2$) of each Bragg peak.

Crystal Structure Solution Methodology: The positions of the Bragg peaks were indexed in terms of their Laue indices by using the formalism developed by Simbrunner et al.[62] The peak positions observed in the GIXRD measurements were combined with the specular diffraction peak to split the indexing procedure into two subsequent steps. First, the lattice constants a, b, and γ of the crystallographic unit cell were determined together with the Laue indices h,k of each Bragg peak. The second step specifies the remaining lattice constants c, α, and β together with the missing Laue indices of the Bragg peaks. A further outcome of the indexing procedure are the Miller indices of the crystallographic plane, which is formed parallel to the substrate surface. The public domain software *GIDInd* was used for the indexing procedure.[63]

In the case of a MOF, the solution of the crystal structure determines the internal framework structure, i.e., the position of the metal nodes and the linker. A suitable guess of the arrangement of the metal nodes within the crystallographic unit cell can be obtained by the "Heavy Atom Method."[64] The high electron density of the metal nodes can be identified by maxima in the Patterson functions. On the one hand, the Patterson function $P(\vec{u})$ can be derived from an autocorrelation of the total electron density, expressed by a convolution of $\rho(\vec{r})$ and $\rho(\vec{r}+\vec{u})$, the same electron density, but translated by the displacement $\vec{u}$.

$$P(\vec{u}) = \iiint_0^1 \rho(\vec{r}) \cdot \rho(\vec{r}+\vec{u})\, dx\, dy\, dz \tag{1}$$

where both the coordinate variables $\vec{r} = (x,y,z)$ as well as the displacement variables $\vec{u} = (u,v,w)$ would be fractions of the crystal lattice vectors for simplicity, which also leads to the adjusted integration boundaries [0,1]. On the other hand, $P(\vec{u})$ can be expressed based on the square of the structure factors $|F_{hkl}|^2$ which are experimental quantities related to the intensity of the Bragg peaks[65]

$$P(\vec{u}) = \frac{1}{V_c} \sum_{hkl} |F_{hkl}|^2 \cos(2\pi(h \cdot u + k \cdot v + l \cdot w)) \tag{2}$$

with the indices hkl referring to diffraction maxima located in the upper hemisphere of detection, conveniently coinciding with the reciprocal space region investigated in GIXRD experiments. While function maxima of the electron density $\rho(\vec{r})$ appear directly at coordinates $\vec{r}$, which are consequently atomic positions, in the Patterson function $P(\vec{u})$ maxima occur at displacement vectors $\vec{u}$, whenever these correspond to relative coordinates between any pair of atoms. The maximum in the Patterson function is proportional to the product of the atomic numbers of the pair of involved atoms. Generally, Patterson functions can be used for the determination of the relative position of heavy atoms, if

$$\frac{\sum_{\text{heavy atoms}} Z_j^2}{\sum_{\text{light atoms}} Z_i^2} > 1 \tag{3}$$

where the sums are taken over all heavy atoms (and light atoms) present in the crystallographic unit cell.[66,67] Here, Z_i and Z_j are the atomic numbers of the atoms.

Although the calculation of Patterson functions was fundamentally explored, an elementary method implemented in a *Matlab* routine was developed for this work. Central to the routine is the implementation of the Fourier series of the square of the structure factors [Equation (2)], where an array of Patterson function values is calculated for a mesh of discrete values for $\vec{u} = (u,v,w)$. These 3D function maps can then be graphically visualized, or peaks could be automatically registered by a rudimentary maxima search.

After positioning the copper atoms within the crystallographic unit cell, the INA linkers were placed in between. The specific connectivity between the copper atoms was identified based on the Patterson map together with known distances from previously reported Cu-INA MOFs crystal structures, as well as by symmetry considerations implied by the diffraction pattern.

A final quality check of the crystal structure solution was performed by the comparison of the calculated peak positions and their structure factors $|F(hkl)|^2$ with the experimentally observed diffraction pattern. These theoretical peak positions were plotted directly on the experimental RSM.

Supporting Information

Supporting Information is available from the Wiley Online Library or from the author.

Acknowledgements

Financial support was given by the Austrian Science Fund FWF [P34463]. V.R.-G. thanks the Research Foundation Flanders (FWO Vlaanderen) for

a Junior Postdoctoral Fellowship (12Z6520N). R.A. acknowledges FWO Vlaanderen for support through the research project G085720N. The authors acknowledge Elettra Sincrotrone Trieste for providing access to its synchrotron radiation facilities (proposals 20180092, 20180105, and 20200226) and thank Luisa Barba and Nicola Demitri for assistance using beamline XRD1. The research leading to this result was supported by the project CALIPSOplus under Grant Agreement 730872 from the EU Framework Programme for Research and Innovation HORIZON 2020. The authors acknowledge support from the European Research Council under the European Union's Horizon 2020 Program (FP/2014-2020)/ERC Grant Agreement No. 771834—POPCRYSTAL and TU Graz for the Lead Project LP-03: Porous Materials @ Work for Sustainability.

Conflict of Interest

The authors declare no conflict of interest.

Data Availability Statement

The data that support the findings of this study are available via https://doi.org/10.3217/1fhne-emd40.

Keywords

chemical vapor deposition, Heavy Atom Method, metal-organic frameworks, Patterson functions, polymorphism

Received: January 9, 2023
Revised: January 31, 2023
Published online: March 28, 2023

[1] S. R. Batten, N. R. Champness, X.-M. Chen, J. Garcia-Martinez, S. Kitagawa, L. Öhrström, M. O'Keeffe, M. P. Suh, J. Reedijk, *Pure Appl. Chem.* **2013**, *85*, 1715.
[2] A. Bavykina, N. Kolobov, I. S. Khan, J. A. Bau, A. Ramirez, J. Gascon, *Chem. Rev.* **2020**, *120*, 8468.
[3] D. Yang, B. C. Gates, *ACS Catal.* **2019**, *9*, 1779.
[4] M. Ding, R. W. Flaig, H.-L. Jiang, O. M. Yaghi, *Chem. Soc. Rev.* **2019**, *48*, 2783.
[5] X. Zhao, Y. Wang, D. Li, X. Bu, P. Feng, *Adv. Mater.* **2018**, *30*, 1705189.
[6] B. Yeskendir, J.-P. Dacquin, Y. Lorgouilloux, C. Courtois, S. Royer, J. Dhainaut, *Mater. Adv.* **2021**, *2*, 7139.
[7] I. Stassen, N. Burtch, A. Talin, P. Falcaro, M. Allendorf, R. Ameloot, *Chem. Soc. Rev.* **2017**, *46*, 3185.
[8] M. D. Allendorf, R. Dong, X. Feng, S. Kaskel, D. Matoga, V. Stavila, *Chem. Rev.* **2020**, *120*, 8581.
[9] C. Crivello, S. Sevim, O. Graniel, C. Franco, S. Pané, J. Puigmartí-Luis, D. Muñoz-Rojas, *Mater. Horiz.* **2021**, *8*, 168.
[10] D. Gentili, M. Gazzano, M. Melucci, D. Jones, M. Cavallini, *Chem. Soc. Rev.* **2019**, *48*, 2502.
[11] A. O. F. Jones, C. Röthel, R. Lassnig, O. N. Bedoya-Martínez, P. Christian, I. Salzmann, B. Kunert, A. Winkler, R. Resel, *CrystEngComm* **2017**, *19*, 1902.
[12] V. Rubio-Giménez, S. Tatay, C. Martí-Gastaldo, *Chem. Soc. Rev.* **2020**, *49*, 5601.
[13] L. Heinke, H. Gliemann, P. Tremouilhac, C. Wöll, in *The Chemistry of Metal–Organic Frameworks: Synthesis, Characterization, and Applications*, (Ed: E. Kasel) Vol. *2*, John Wiley & Sons, **2016**, p. 523.
[14] Z. Wang, C. Wöll, *Adv. Mater. Technol.* **2019**, *4*, 1800413.
[15] J. Liu, B. Lukose, O. Shekhah, H. K. Arslan, P. Weidler, H. Gliemann, S. Bräse, S. Grosjean, A. Godt, X. Feng, K. Müllen, I.-B. Magdau, T. Heine, C. Wöll, *Sci. Rep.* **2012**, *2*, 921.
[16] H. K. Arslan, O. Shekhah, D. C. F. Wieland, M. Paulus, C. Sternemann, M. A. Schroer, S. Tiemeyer, M. Tolan, R. A. Fischer, C. Wöll, *J. Am. Chem. Soc.* **2011**, *133*, 8158.
[17] S. Liu, S. Shinde, J. Pan, Y. Ma, Y. Yan, G. Pan, *Chem. Eng. J.* **2017**, *324*, 216.
[18] Z.-G. Gu, J. Zhang, *Coord. Chem. Rev.* **2019**, *378*, 513.
[19] V. Rubio-Giménez, M. Galbiati, J. Castells-Gil, N. Almora-Barrios, J. Navarro-Sánchez, G. Escorcia-Ariza, M. Mattera, T. Arnold, J. Rawle, S. Tatay, E. Coronado, C. Martí-Gastaldo, *Adv. Mater.* **2018**, *30*, 1704291.
[20] P. Falcaro, K. Okada, T. Hara, K. Ikigaki, Y. Tokudome, A. W. Thornton, A. J. Hill, T. Williams, C. Doonan, M. Takahashi, *Nat. Mater.* **2017**, *16*, 342.
[21] B. Baumgartner, K. Ikigaki, K. Okada, M. Takahashi, *Chem. Sci.* **2021**, *12*, 9298.
[22] A. Tanskanen, M. Karppinen, *Sci. Rep.* **2018**, *8*, 8976.
[23] A. Khayyami, A. Philip, M. Karppinen, *Angew. Chem., Int. Ed.* **2019**, *58*, 13400.
[24] M. Tu, D. E. Kravchenko, B. Xia, V. Rubio-Giménez, N. Wauteraerts, R. Verbeke, I. F. Vankelecom, T. Stassin, W. Egger, M. Dickmann, *Angew. Chem., Int. Ed.* **2021**, *60*, 7553.
[25] D. W. Bennett, *Understanding Single-Crystal X-Ray Crystallography*, Wiley, New York **2010**.
[26] R. Černý, *Crystals* **2017**, *7*, 142.
[27] A. I. Kitaigorodskii, *Acta Crystallogr.* **1965**, *18*, 585.
[28] A. Burger, R. Ramberger, *Microchim. Acta* **1979**, *72*, 259.
[29] C. Lercher, C. Röthel, O. M. Roscioni, Y. H. Geerts, Q. Shen, C. Teichert, R. Fischer, G. Leising, M. Sferrazza, G. Gbabode, R. Resel, *Chem. Phys. Lett.* **2015**, *630*, 12.
[30] L. Pithan, D. Nabok, C. Cocchi, P. Beyer, G. Duva, J. Simbrunner, J. Rawle, C. Nicklin, P. Schäfer, C. Draxl, F. Schreiber, S. Kowarik, *J. Chem. Phys.* **2018**, *149*, 144701.
[31] S. Yuan, P. Zhang, L. Zhang, A. T. Garcia-Esparza, D. Sokaras, J.-S. Qin, L. Feng, G. S. Day, W. Chen, H. F. Drake, P. Elumalai, S. T. Madrahimov, D. Sun, H.-C. Zhou, *J. Am. Chem. Soc.* **2018**, *140*, 10814.
[32] J. Zhou, X. Tan, F. Hu, H.-H. Zou, F. A. Almeida Paz, L. Fu, R. Zhao, *Dalton Trans.* **2016**, *45*, 11292.
[33] H. Hou, Z. Liu, CCDC deposition number: 1241445, **2004**.
[34] L. Tang, Y. P. Wu, F. Fu, W. L. Wang, Y. Y. Lian, F. Hu, A. M. Bai, *Acta Chim. Sin.* **2010**, *68*, 1261.
[35] J. Y. Lu, A. M. Babb, *Chem. Commun.* **2002**, 1340.
[36] Y.-H. Liu, Y.-L. Lu, H.-L. Tsai, J.-C. Wang, K.-L. Lu, *J. Solid State Chem.* **2001**, *158*, 315.
[37] M. E. Chapman, P. Ayyappan, B. M. Foxman, G. T. Yee, W. Lin, *Cryst. Growth Des.* **2001**, *1*, 159.
[38] M.-L. Tong, L.-J. Li, K. Mochizuki, H.-C. Chang, X.-M. Chen, Y. Li, S. Kitagawa, *Chem. Commun.* **2003**, 428.
[39] F.-P. Liang, S.-N. Qin, C.-F. Jiang, Z. Zhang, Z.-L. Chen, *Organometallics* **2007**, *26*, 4839.
[40] D. Ghosh, K. Ferfolja, Ž. Drabavičius, J. W. Steed, K. K. Damodaran, *New J. Chem.* **2018**, *42*, 19963.
[41] B. Zhai, L.-L. Song, W.-J. Wang, Z.-Y. Li, S.-Z. Li, F.-L. Zhang, C. Zhang, Y.-B. Zang, *J. Solid State Chem.* **2018**, *264*, 29.
[42] B. Liu, L. Xu, G. Guo, *J. Solid State Chem.* **2006**, *179*, 883.
[43] J. Jiang, Z. Lu, M. Zhang, J. Duan, W. Zhang, Y. Pan, J. Bai, *J. Am. Chem. Soc.* **2018**, *140*, 17825.
[44] M. Almáši, Z. Vargová, R. Gyepes, R. Varga, V. Zeleňák, *Inorg. Chem. Commun.* **2014**, *46*, 118.
[45] A. Kondo, H. Noguchi, H. Kajiro, T. Ohba, K. Kaneko, H. Kanoh, *Langmuir* **2008**, *24*, 170.
[46] J. Y. Lu, A. M. Babb, *Chem. Commun.* **2001**, 821.
[47] M. Linares-Moreau, L. A. Brandner, T. Kamencek, S. Klokic, F. Carraro, K. Okada, M. Takahashi, E. Zojer, C. J. Doonan, P. Falcaro, *Adv. Mater. Interfaces* **2021**, *8*, 2101039.

[48] T. Stassin, S. Rodríguez-Hermida, B. Schrode, A. J. Cruz, F. Carraro, D. Kravchenko, V. Creemers, I. Stassen, T. Hauffman, D. De Vos, P. Falcaro, R. Resel, R. Ameloot, *Chem. Commun.* **2019**, *55*, 10056.
[49] A. J. Cruz, I. Stassen, M. Krishtab, K. Marcoen, T. Stassin, S. Rodríguez-Hermida, J. Teyssandier, S. Pletincx, R. Verbeke, V. Rubio-Giménez, S. Tatay, C. Martí-Gastaldo, J. Meersschaut, P. M. Vereecken, S. De Feyter, T. Hauffman, R. Ameloot, *Chem. Mater.* **2019**, *31*, 9462.
[50] I. Stassen, M. Styles, G. Grenci, H. V. Gorp, W. Vanderlinden, S. D. Feyter, P. Falcaro, D. D. Vos, P. Vereecken, R. Ameloot, *Nat. Mater* **2016**, *15*, 304.
[51] J.-K. Huang, N. Saito, Y. Cai, Y. Wan, C.-C. Cheng, M. Li, J. Shi, K. Tamada, V. C. Tung, S. Li, L.-J. Li, *ACS Mater. Lett.* **2020**, *2*, 485.
[52] M. Kräuter, A. J. Cruz, T. Stassin, S. Rodríguez-Hermida, R. Ameloot, R. Resel, A. M. Coclite, *Crystals* **2022**, *12*, 217.
[53] P. Zaumseil, *J. Appl. Crystallogr.* **2015**, *48*, 528.
[54] Y. Cudennec, A. Lecerf, *Solid State Sci.* **2003**, *5*, 1471.
[55] V. Rubio-Giménez, G. Arnauts, M. Wang, E. S. Oliveros Mata, X. Huang, T. Lan, M. L. Tietze, D. E. Kravchenko, J. Smets, N. Wauteraerts, A. Khadiev, D. V. Novikov, D. Makarov, R. Dong, R. Ameloot, *J. Am. Chem. Soc.* **2023**, *145*, 152.
[56] T. Stassin, S. Rodríguez-Hermida, B. Schrode, A. J. Cruz, F. Carraro, D. Kravchenko, V. Creemers, I. Stassen, T. Hauffman, D. De Vos, P. Falcaro, R. Resel, R. Ameloot, *Chem. Commun.* **2019**, *55*, 10056.
[57] C. J. Heffelfinger, P. G. Schmidt, *J. Polym. Sci.* **1960**, *47*, 289.
[58] C. Detavernier, C. Lavoie, *Materials Science Forum*, Trans Tech Publications, 495–497 **2005**, pp. 1333–1342.
[59] Y. Yoneda, *Phys. Rev.* **1963**, *131*, 2010.
[60] K. Waizump, M. Takuno, N. Fukushima, H. Masuda, *J. Coord. Chem.* **1998**, *44*, 269.
[61] B. Schrode, S. Pachmajer, M. Dohr, C. Röthel, J. Domke, T. Fritz, R. Resel, O. Werzer, *J. Appl. Crystallogr.* **2019**, *52*, 683.
[62] J. Simbrunner, C. Simbrunner, B. Schrode, C. Röthel, N. Bedoya-Martinez, I. Salzmann, R. Resel, *Acta Crystallogr., Sect. A: Found. Adv.* **2018**, *74*, 373.
[63] M. P. Kainz, L. Legenstein, V. Holzer, S. Hofer, M. Kaltenegger, R. Resel, J. Simbrunner, *J. Appl. Crystallogr.* **2021**, *54*, 1256.
[64] D. Harker, *J. Chem. Phys.* **1936**, *4*, 381.
[65] A. L. Patterson, *Phys. Rev.* **1934**, *46*, 372.
[66] U. Shmueli, *International Tables for Crystallography , Vol. B - Reciprocal Space*, (Ed: U. Shmueli) Kluwer Academic Publishers **1996**.
[67] M. G. Rossmann, *Acta Crystallogr., Sect. A: Found. Adv.* **1996**, *52*, C570.